Robust Ferromagnetism of Chromium Nanoparticles Formed in Superfluid Helium

Shengfu Yang,* Cheng Feng, Daniel Spence, Aula M. A. A. Al Hindawi, Elspeth Latimer, Andrew M. Ellis, Chris Binns, Davide Peddis, Sarnjeet S. Dhesi, Liying Zhang, Yafei Zhang, Kalliopi N. Trohidou,* Marianna Vasilakaki, Nikolaos Ntallis, Ian MacLaren, and Frank M. F. de Groot

First postulated by Louis Néel in 1936,[1] antiferromagnetic ordering in elemental chromium was confirmed in 1953 by neutron diffraction.[2] The antiparallel alignment of atomic magnetic moments in bulk chromium results in properties such as near-zero net magnetization and very high resistance against magnetization when subjected to an external magnetic field. On the surfaces of chromium crystals and chromium thin films ferromagnetism can exist,[3–7] although the bulk chromium remains antiferromagnetic. In contrast, free chromium clusters composed of a few atoms to hundreds of atoms can have non-zero and structure-dependent magnetic moments. For instance, chromium clusters composed of 58 chromium atoms in the gas phase have been found with a magnetic moment as high as 1.16 μ_B/atom, which then decreases toward the bulk limit (zero net magnetization) as the cluster size increases.[8,9] However, ferromagnetic ordering in these clusters is intrinsically unstable when they are deposited on a substrate. Although single chromium atoms show a large spin magnetic moment (4.5 μ_B/atom) on an Au(111) surface, their aggregates always manifest vanishingly small magnetization.[10] So far a switch to ferromagnetic ordering in chromium remains elusive.

Antiferromagnetic materials are known to exhibit weak magnetization at the nanoscale because of uncompensated spins[11] and/or canted spins[12] at the surfaces. Strong ferromagnetism can be obtained in antiferromagnetic materials, in particular metal oxides, by structural strain and/or defects.[13,14] This is because the enlarged inter-atomic distance at these sites reduces the overlap of d orbitals of transition metals, leading to enhanced magnetism by mimicking single atoms. However, in the case of chromium all of the nanoparticles previously deposited on surfaces, including pure chromium nanoparticles and the stable oxide, Cr_2O_3, have been found to be antiferromagnetic,[12,15–18] and so far there is no evidence that they can be switched into a ferromagnetic state at the nanoscale.

Here, we report on the production of chromium nanoparticles by the addition of chromium atoms to superfluid helium droplets. The chromium atoms were generated by evaporating solid chromium in an oven and allowing the vapor to collide with a beam of liquid helium droplets.[19] The superfluidity of the droplets then allowed chromium atoms to migrate in a frictionless manner and coagulate into nanoparticles. The resulting chromium particles grown inside these droplets

S. Yang, C. Feng, D. Spence, A. M. A. A. Al Hindawi,
E. Latimer, A. M. Ellis
Department of Chemistry
University of Leicester
Leicester LE1 7RH, UK
E-mail: sfy1@le.ac.uk
C. Binns
Department of Physics and Astronomy
University of Leicester
Leicester LE1 7RH, UK
D. Peddis
Institute of Structure of Matter
National Research Council (CNR)
00015 Monterotondo Scalo, Italy
S. S. Dhesi
Diamond Light Source
Harwell Science and Innovation Campus
Didcot OX11 0DE, UK
L. Zhang, Y. Zhang
School of Electronics
Information and Electrical Engineering
Shanghai Jiaotong University
Shanghai 200240, China

K. N. Trohidou, M. Vasilakaki, N. Ntallis
Institute of Nanoscience and Nanotechnology
NCSR Demokritos
153 10 Aghia, Greece
E-mail: k.trohidou@inn.demokritos.gr
N. Ntallis
Department of Physics
Aristotle University
54124 Thessaloniki, Greece
I. MacLaren
Department of Physics and Astronomy
University of Glasgow
Glasgow G12 8QQ, UK
F. M. F. de Groot
Department of Chemistry
Utrecht University
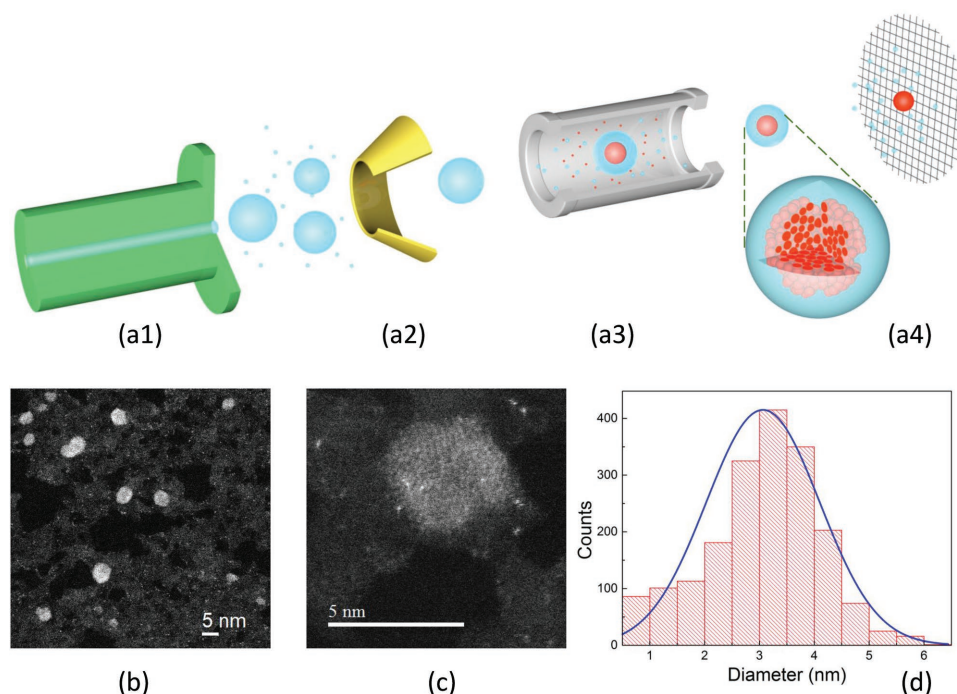Universiteitsweg 99, 3584CG Utrecht, The Netherlands

Figure 1. Schematic of the apparatus and formation of chromium nanoparticles. a) The UHV helium droplet source used to synthesize chromium nanoparticles, including (a1) a low-temperature nozzle that allows expansion of pre-cooled high pressure helium gas, (a2) a skimmer for collimating the helium droplet beam, (a3) a high-temperature oven for producing chromium vapor, and (a4) the particle deposition region. The expanded view in (a4) illustrates a disordered chromium nanoparticle embedded in a single helium droplet. b) HAADF-STEM image showing the diverse morphology. c) Magnified HAADF-TEM image of a chromium nanoparticle showing disorder in structure. d) Size distribution of chromium nanoparticles with a mean diameter of 3.1 ± 1.0 nm.

were then transferred onto a deposition target by collision of the droplet with the target. The deposition target was subsequently removed from vacuum for investigations. Two sets of chromium nanoparticles with slightly different sizes were prepared, one with a mean diameter of 2.4 ± 1.1 nm and the other 3.1 ± 1.0 nm. **Figure 1** presents a schematic showing how the chromium nanoparticles were made, as well as information on the particle size, morphology, and size distribution, which was obtained using high angle annular dark field scanning transmission electron microscopy (HAADF-STEM). Rather than a spherical single crystalline or polycrystalline structure, as seen for some noble metal nanoparticles grown in helium droplets,[20–22] STEM images show that the chromium nanoparticles vary in morphology, as well as being highly disordered at the atomic scale (see Figure 1b,c). The disorder can lead to defects at the surface, as well as in the interior of the chromium nanoparticles.

In order to determine the magnetic properties of the nanoparticles, we first performed an X-ray absorption spectroscopy (XAS) measurement at the $L_{2,3}$ edge of chromium, from which X-ray magnetic circular dichroism (XMCD) spectra were obtained (see **Figure 2**). Sum rules[23,24] were then applied to estimate the spin and orbital magnetic moments. To correct for the overlap of the L_2 and L_3 spectra, a spin correction factor of 1.5 was employed, which was calculated from the relative intensities of the L_2 and L_3 peaks.[25,26] The integrals of the XAS spectrum after the edge-jump corrections and the XMCD spectrum

yield a spin moment of 0.83 μ_B/atom and an orbital moment of 0.10 μ_B/atom at 1.5 K.

Oxidation at the surface is inevitable when chromium nanoparticles are removed from vacuum and transported for ex situ investigations, as was done here. Evidence for oxidation is also available from the XMCD spectrum in Figure 2c. To ascertain whether quadrivalent or trivalent chromium oxides were formed, crystal field multiplet calculations[27] were performed to calculate the XAS spectra with left and right polarized X-rays, and the resulting theoretical XMCD spectrum is compared with the experimental spectrum in Figure 2c (normalized to the 575.6 eV peak). We have found that the experimental XAS spectrum can be well described with a Cr^{3+} state of $^4A_2$ symmetry. Since this (ground) state is also found in Cr_2O_3, the simulation suggests that the magnetic chromium nanoparticles contain an effective ferro(i)magnetic trivalent oxide species. Note that the experimental and theoretical spectra in Figure 2c are not in perfect agreement, and some pure chromium is likely deeper inside the nanoparticles.

The XMCD measurement shows that the chromium nanoparticles are strongly magnetic. However, the sum rules are known to underestimate the magnetic moments for light transition metals;[28] hence we directly measured magnetic moments of chromium nanoparticles using a superconducting quantum interference device (SQUID). **Figure 3** shows the hysteresis curves of chromium nanoparticles measured at different temperatures, which show responses expected for
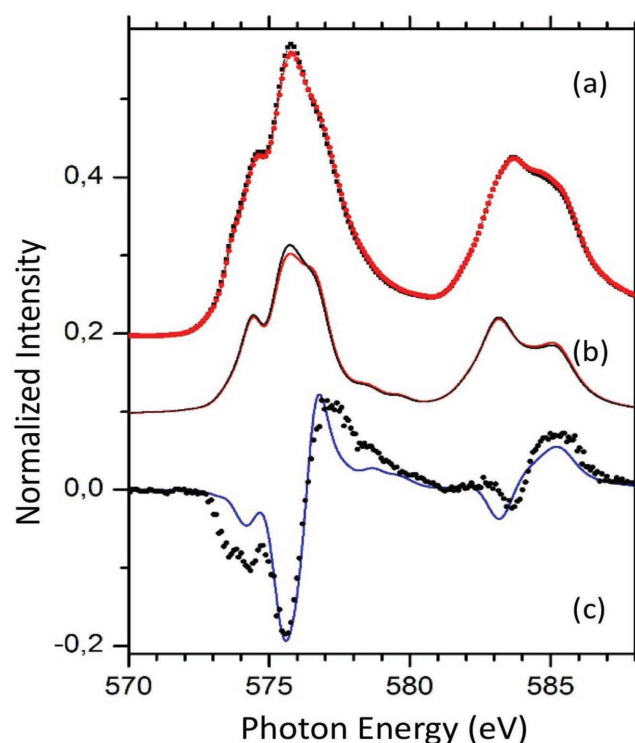
Figure 2. $L_{2,3}$-edge XAS and XMCD spectra of chromium nanoparticles. a) The XAS spectra of chromium measured with left (red) and right (black) polarized X-rays. b) The calculated XAS spectra from a crystal field multiplet calculation with left (red) and right (black) polarized X-rays. c) The experimental (black) and the normalized theoretical (blue) XMCD spectra.

ferromagnetism. The $M–H$ curves are found to saturate at modest magnetic fields, i.e., ≈5 T at low temperatures and less than 1 T at room temperature for both samples. Saturation magnetizations observed are close to those of ferromagnetic cobalt and iron and are significantly higher than for any chromium nanoparticles previously reported.[15,18] Figure 3a shows the $M–H$ curves of chromium nanoparticles with a mean diameter of 2.4 nm. These particles possess magnetic moments as high as

1.29 μ_B/atom at 5 K and 0.45 μ_B/atom at 300 K. In the expanded view, we show the magnetic properties of chromium nanoparticles at low field, yielding reduced remanent magnetizations (M_r/M_s) of 0.083 at 5 K and 0.089 at 300 K, respectively. Figure 3b shows the hysteresis curves of chromium nanoparticles with a mean diameter of 3.1 nm measured at different temperatures. At 3, 4, and 5 K, the magnetic moments are 1.83, 1.57, and 1.12 μ_B/atom, respectively, and the magnetic moment is 0.30 μ_B/atom at 300 K. Compared with chromium particles with a diameter of 2.4 nm, the magnetic moments are slightly lower at the same temperatures. For both sizes paramagnetic behavior starts at temperatures higher than those reported for larger Cr nanoparticles.[6,7]

The temperature dependence of the saturation magnetization (M_s) of chromium nanoparticles was also investigated in order to gain further information on the magnetism of chromium nanoparticles. The saturation magnetization was obtained from the $M–H$ curves of chromium nanoparticles with a diameter of 3.1 nm measured across the temperature range 3–300 K. As seen in **Figure 4**a, at the lowest temperatures M_s decreases rapidly as the temperature increases from 1.83 μ_B/atom at 3 K to a minimum of 0.25 μ_B/atom at 10 K. The magnetization then remains constant between 10 and 50 K and begins to increase at higher temperature, reaching a peak value at ~100 K with a saturation magnetization of ~0.70 μ_B/atom. Above 100 K the saturation magnetization monotonically decreases with temperature and reaches a value of 0.30 μ_B/atom at 300 K. As detailed later, the temperature-dependent magnetization is fully in line with defect-rich pure chromium in the core of the nanoparticles according to Monte Carlo simulations.[29]

In stark contrast to previous experiments,[12,15–18] the observation of strong magnetism in chromium nanoparticles is unprecedented. The different behavior we see is likely to be due to the structural disorder in chromium nanoparticles at the atomic scale, as displayed by TEM images (see Figure 1c). Disorder can cause strains and/or defects in nanomaterials and can significantly increase the proportion of uncompensated spins, producing a high imbalance in the spin sub-lattices and thus a high saturation magnetization for the nanoparticles. Indeed, strains and/or defects can cause a transition from antiferromagnetism to ferromagnetism for the Cr_2O_3 component
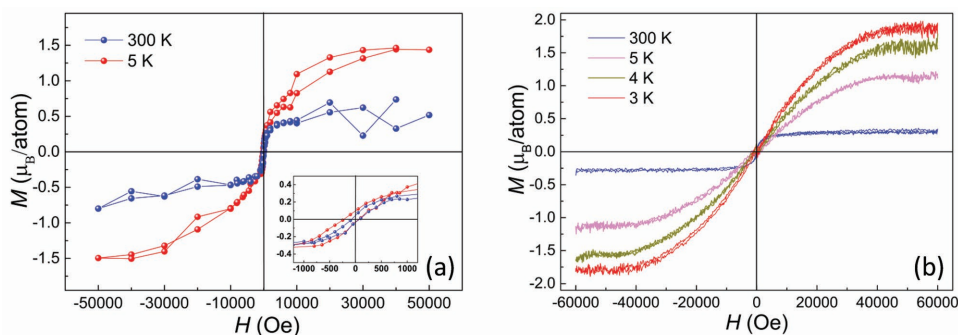

Figure 3. Magnetic properties of chromium nanoparticles measured using SQUID. a) Hysteresis curves of chromium nanoparticles with a diameter of 2.4 nm, measured at 5 and 300 K, respectively. The inset shows an expanded view of the $M–H$ curves at low field. b) Hysteresis curves of chromium nanoparticles with a diameter of 3.1 nm, measured at 3, 4, 5, and 300 K, respectively. At room temperature, the magnetization saturated when subjected to an external field of <0.5 T, while at lower temperature a stronger external field was needed (4–5 T).
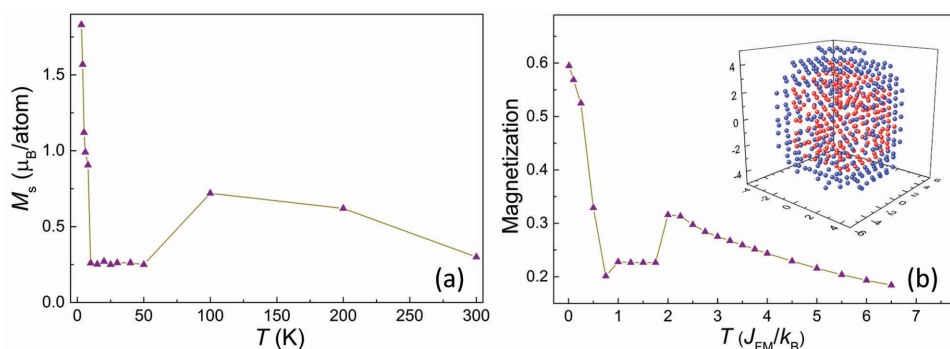
Figure 4. Temperature-dependent saturation magnetization of chromium nanoparticles. a) The saturation magnetization of chromium nanoparticles with a diameter of 3.1 nm measured in the temperature range of 3–300 K. For each data point the hysteresis curve was first measured from which the saturation magnetization was derived. b) Monte Carlo simulation of the temperature-dependent magnetization with an external field of $H_{FC} = 0.4\ J_{FM}/\mu_B$. In the inset, the model nanoparticle has a total radius of five lattice spacings with 185 defects (114 in the core and 71 at the surface) and has 309 surface spins (blue) and 191 core spins (red).

of the particles, with precedent from other antiferromagnetic metal oxides, such as $LuMnO_3$[13] and NiO.[14] For pure chromium, we have performed Monte Carlo simulations on isolated chromium nanoparticles with a diameter of ~2.9 nm (taking the chromium lattice constant as 0.288 nm) to confirm this landscape. The model nanoparticle has a total radius of five lattice spacings imposed on a simple cubic lattice (see the inset of Figure 4b) and a surface thickness of one lattice spacing. By removing spins randomly from some lattice sites we generated defects in the core and at the surface. The magnetization curves were then calculated during a field heating procedure starting at the temperature $T = 0.01\ J_{FM}/k_B$ to $T = 6.5\ J_{FM}/k_B$ at a constant rate under a static magnetic field H_{FC} directed along the easy axis (i.e., the z-axis).

As seen in Figure 4b, the general behavior across the simulated temperature range bears a strong resemblance to the experimental plot, with large magnetization at low temperature region that initially decreases rapidly with the increase of temperature before levelling off. The magnetization starts to increase significantly at higher temperature owing to thermo-induced magnetization (TIM).[30–32] As the temperature increases loose spins in the nanoparticles (which are the surface spins and the spins around the defects) start to fluctuate. Because of the very small anisotropy (as seen in the expanded view of Figure 2a), these spins can flip and gradually change the sub-lattice, leading to enhanced magnetization. The enhancement of magnetization and the range of temperatures where this enhancement occurs depend sensitively on the nanoparticle size, the magnitude and type of magnetic anisotropy, and the size of the exchange anisotropy, if present. A further increase of temperature results in large fluctuations of all the spins, which reduces the magnetization until it vanishes as the temperature approaches the Néel temperature (T_N). The Monte Carlo simulation confirms that chromium nanoparticles with abundant defects can be strongly ferromagnetic.

Finally, we discuss why chromium nanoparticles formed in superfluid helium can be highly disordered at the atomic scale. Unlike conventional growth methods, the nanoparticles are formed by adding chromium atoms to helium droplets one by one, which then aggregate inside the very cold superfluid

(which has a steady-state temperature of 0.37 K[19]). This process can yield crystalline structures for some types of nanoparticles. Examples include fcc structures for Ag—Au bimetallic nanoparticles[20] and decahedral, icosahedral, and fcc structures in pure Ag nanoparticles.[21] The disorder in chromium nanoparticles might be related to the antiferromagnetic nature of chromium atoms and its effect on particle growth in superfluid helium. When the first two chromium atoms are added to a helium droplet, they will naturally align with antiparallel spins and form a chromium dimer in its ground electronic state ($X^1\Sigma_g^+$).[33] As a third chromium atom enters the droplet and approaches the chromium dimer, it can interact with a nearby atom via either antiferromagnetic or ferromagnetic coupling. The ferromagnetic coupling has a higher energy than the antiferromagnetically coupled structure; hence, the exchange interaction will tend to keep the two atoms apart and the atoms will be separated by a longer distance than the antiferromagnetically coupled atoms, which is different from that expected in a fully annealed bcc structure. To provide support for this mechanism, we have calculated all three stable structures of the Cr_3 cluster using the Vienna Ab initio Simulation Package (VASP);[34] the structures are illustrated in **Figure 5**. Our calculation confirms that when atoms 1 and 3 have parallel spins they have to be further apart than the antiparallel spin distance in order to be in an energetically favorable state. Since any excess energy will be rapidly removed by the superfluid helium, leaving no energy to re-arrange the overall structure, a highly frustrated aggregation procedure results. This process continues as the nanoparticle grows, producing a nanoparticle with defects in the absence of any annealing.

In summary, strong ferromagnetic ordering in chromium nanoparticles has been reported for the first time. For the two batches of nanoparticles investigated, we find that smaller nanoparticles possess higher magnetic moment than larger ones. The chromium nanoparticles contain both Cr_2O_3 and pure chromium components, which have been confirmed by simulations. Both components contribute to the ferromagnetism due to greatly increased unbalanced surface spins in chromium nanoparticles, although the exact contribution to the overall ferromagnetism from each component cannot be distinguished in
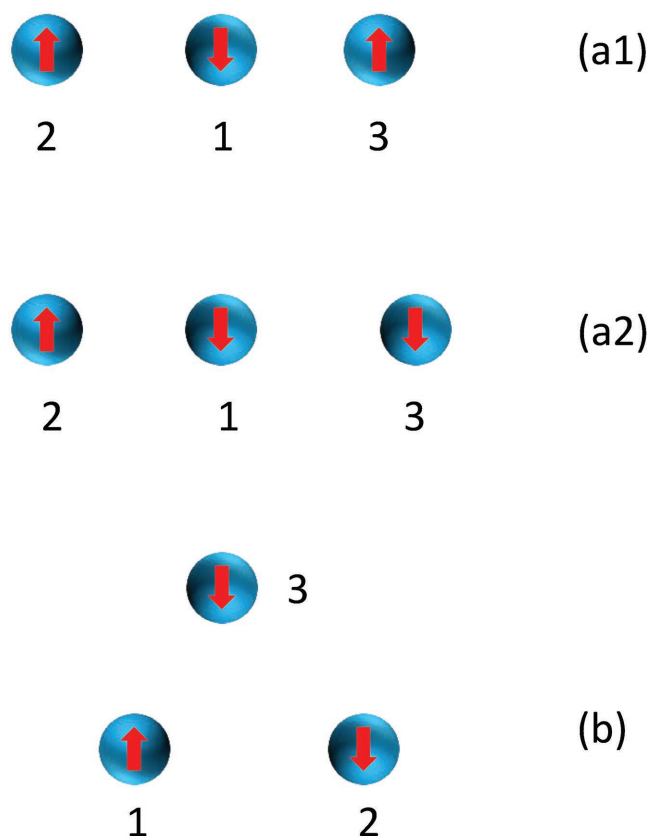
Figure 5. Structures and spin orientations from VASP calculations of chromium trimers. In all cases, atoms 1 and 2 are kept at the lattice distance of bulk chromium and in an antiferromagnetic configuration. Atom 3 is displaced until all three atoms have comparable magnetic moments with either up or down orientation and the stable structures are reached. (a1) Linear structure with up-down-up spins, with $d_{12} = 1$ and $d_{23} = 1$; (a2) Linear structure with up-down-down spins, with $d_{12} = 1$ and $d_{23} = 1.28$; b) Nonlinear structure with $d_{12} = 1$, $d_{13} = 0.89$, and $d_{23} = 1$, respectively. The distances are measured in units of the bulk Cr lattice constant ~2.9 Å, and an overall magnetic moment with a magnitude of $4.5 \pm 0.3\ \mu_B$ is obtained for all of the structures.

this work. To explain the disorder at the atomic scale a highly frustrated growth mechanism in superfluid helium droplets has been proposed, which is verified by theoretical modeling. In this process, the exchange interaction between chromium atoms plays a central role as the particle grows, atom-by-atom, in the cold superfluid helium. This implies that antiferromagnetic elements, such as chromium and manganese, can potentially be incorporated into novel types of nanomagnets, for example, with ferromagnetic materials filling the defects of the antiferromagnetic materials. Experiments have shown that chromium diluted in other materials can exhibit ferromagnetism, for example, with a concentration <7% in ZnO.[35] Our experiment suggests that a much higher concentration of chromium can also give rise to enhanced ferromagnetism if the structure is properly tailored. Such materials may offer new properties, *e.g.*, greater magnetization and tunable coercivity. On the other hand, the mechanism for the robust ferromagnetic ordering in chromium nanoparticles, which involves highly frustrated aggregation driven by exchange interactions

with minimal thermal influence, suggests a new route for the fabrication of high-moment magnetic nanomaterials using superfluid helium droplets as the growth medium. If ferromagnetic elements are used instead of chromium, the atoms are expected to aggregate with maximal atomic spins (nearly all populated in the ground electronic states at the temperature close to 0 K) aligned in a parallel fashion (due to the exchange interaction), resulting in materials with much enhanced magnetization. Hence, superfluid helium has the potential to become an exciting new solvent in which to synthesize nanomaterials with very high magnetic moments.

Experimental Section

Particle Synthesis: Helium droplets were formed by continuous expansion of pre-cooled helium into a vacuum chamber via a 5 μm pinhole nozzle.[20] In this work, nozzle temperatures of 9.0 and 8.5 K and a stagnation pressure of 15 bar were used, producing helium droplets composed of 1.5×10^6 and 2.0×10^6 atoms, respectively. As each helium atom can remove 5 cm^{-1} of energy through evaporation,[19] nanoparticles with an average number of up to 580 chromium atoms can be fabricated. The droplets were then skimmed to form a collimated beam and passed through an oven evaporator containing elemental chromium which was resistively heated to 1275 K. The helium droplets captured the chromium atoms and formed nanoparticles inside the droplets. The particles were removed from the droplets by their collision with a substrate at room temperature and the deposition rate was measured by a quartz crystal microbalance. The deposition station consisted of a sample holder, an XYZ sample manipulator, and a load-lock chamber to allow the removal of deposition targets without venting the ultra-high vacuum (UHV) chambers. For TEM imaging and XMCD measurements, the nanoparticles were deposited on lacey carbon TEM grids, while for SQUID measurements polyetheretherketone (PEEK) substrates were employed. For TEM the particles were deposited on the substrates for 5 min whereas for SQUID and XMCD experiments nanoparticles were deposited continuously for 7 h in order to collect a sufficient amount of material for acceptable magnetic measurements.

Characterization Methods: HAADF-STEM images were obtained using a JEOL ARM200F instrument equipped with a cold field emission gun and operated at 200 kV, which can reach atomic resolution. For magnetic properties, both the hysteresis curves and XMCD spectra were measured. For chromium nanoparticles with a diameter of 2.4 nm, hysteresis curves were measured using a Magnetic Properties Measurement System (MPMS XL-5, Quantum Design) at CNR, Rome, which can operate over the temperature range of 5–300 K and a maximum field of 5 T. For the particles with a diameter of 3.1 nm, a Quantum Design Physical Properties Measurement System (PPMS EC-II, Quantum Design) available at Shanghai Jiaotong University was employed. This alternative SQUID system can measure the magnetic properties of particles in the temperature range of 2–400 K and for external fields up to 9 T. XMCD spectra were obtained using total electron yield (TEY) measurements on the superconducting magnet on beamline I06 at the Diamond Light Source, UK. X-ray absorption spectra were recorded by switching between left- and right-circularly polarized light or by reversing the magnetic field. The XMCD spectrum shown in Figure 1d was calculated as the difference between spectra taken with left and right circularly polarized light for nanoparticles with a diameter of 3.1 nm.

Calculations: Simulations on isolated AFM nanoparticles were performed using the Monte Carlo technique. The spins in the particle interact with nearest neighbors through Heisenberg exchange interactions, and at each crystal site they experience a uniaxial anisotropy. In the presence of an external magnetic field the total Hamiltonian of the system is[36,37]

COMMUNICATION

$$H = -J \sum_{<i,j>} \vec{S}_i \cdot \vec{S}_j - K_C \sum_{i \in core} \left(\vec{S}_i \cdot \hat{e}_i \right)^2$$
$$- K_{srf} \sum_{i \in srf} \left(\vec{S}_i \cdot \hat{e}_i \right)^2 - \vec{H} \cdot \sum_i \vec{S}_i \qquad (1)$$

Here, S_i is the atomic spin at site i and $\hat{e}_i$ is the unit vector in the direction of the easy axis. The angular brackets () denote a summation over the nearest neighbor atoms only. The first term in Equation (1) gives the exchange interaction between the spins of the AFM nanoparticle. The exchange coupling constant is considered as $J = -1.0J_{FM}$, where J_{FM} is considered to be the exchange coupling constant of a pure ferromagnet (FM) and $J_{FM} = 1$ is taken as a reference value. The second and the third terms describe the anisotropy energy of the AFM core. The anisotropy constant of the core is $K_C = 0.2J_{FM}$ and that of the AFM surface is $K_{srf} = 1.0J_{FM}$: the latter is larger because of the lower crystal symmetry. Uniaxial anisotropy in the core along the z-axis and radial anisotropy at the surface are considered. The last term in the equation is the Zeeman energy. The applied magnetic field is given in units of J_{FM}/μ_B, T is in units of J_{FM}/k_B, and the anisotropy constants are in units of J_{FM}.

First principles calculations were performed based on spin-polarized density functional theory in order to study magnetic properties of the chromium trimers (see Figure 5). The non-empirical general gradient approximation (GGA) exchange correlation functional proposed by Perdew–Burke–Erzenhof (PBE) was used.[38] The electronic charge density and the local potential were expressed in plane wave basis sets. The interactions between the electrons and ions were described using the projector-augmented wave (PAW) method,[39] as implemented by the VASP.[34] Convergence tests led to energy cutoff of the plane-wave basis of 400 eV. The cell was sampled with a $9 \times 9 \times 9$ k-grid generated by the Monkhorst–Pack method.[40] The accuracy for the total energy minimization is 10^{-5} eV.

Acknowledgements

[1] L. Néel, *C. R. Seances Acad. Sci., Vie Acad.* **1936**, *203*, 304.
[2] C. G. Shull, M. K. Wilkinson, *Rev. Mod. Phys.* **1953**, *25*, 100.
[3] G. Allan, *Phys. Rev. B* **1979**, *19*, 4774.
[4] D. R. Grempel, *Phys. Rev. B* **1981**, *24*, 3928.
[5] L. E. Klebanoff, S. W. Robey, G. Liu, D. A. Shirley, *Phys. Rev. B* **1984**, *30*, 1048.
[6] M. C. Hanf, C. Pirri, J. C. Peruchetti, D. Bolmont, G. Gewinner, *Phys. Rev. B* **1987**, *36*, 4487(R).
[7] L. E. Klebanoff, R. H. Victora, L. M. Falicov, D. A. Shirley, *Phys. Rev. B* **1985**, *32*, 1997.
[8] L. A. Bloomfield, J. Deng, H. Zhang, J. W. Emmert, in *Proceedings of the International Symposium on Cluster and Nanostructure Interfaces* (Eds: P. Jena, S. N. Khanna, B. K. Rao), World Scientific, Singapore **2000**, p. 131.
[9] F. W. Payne, W. Jiang, L. A. Bloomfield, *Phys. Rev. Lett.* **2006**, *97*, 193401.
[10] C. Boeglin, P. Ohresser, R. Decker, H. Bulou, F. Scheurer, I. Chado, S. S. Dhesi, E. Gaudry, B. Lazarovits, *Phys. Status Solidi* **2005**, *242*, 1775.
[11] R. H. Kodama, S. A. Makhlouf, A. E. Berkowitz, *Phys. Rev. Lett.* **1997**, *79*, 1393.
[12] D. Li, Z. Han, J. G. Zheng, X. L. Wang, D. Y. Geng, J. Li, Z. D. Zhang, *J. Appl. Phys.* **2009**, *106*, 053913.
[13] J. S. White, M. Bator, Y. Hu, H. Luetkens, J. Stahn, S. Capelli, S. Das, M. Döbeli, Th. Lippert, V. K. Malik, J. Martynczuk, A. Wokaun, M. Kenzelmann, Ch. Niedermayer, C. W. Schneider, *Phys. Rev. Lett.* **2013**, *111*, 037201.
[14] I. Sugiyama, N. Shibata, Z. Wang, S. Kobayashi, T. Yamamoto, Y. Ikuhara, *Nat. Nanotechnol.* **2013**, *8*, 266.
[15] Y. Tsunoda, H. Nakano, S. Matsuo, *J. Phys.: Condens. Matter* **1993**, *5*, L29.
[16] M. R. Fitzsimmons, J. A. Eastman, R. A. Robinson, J. W. Lynn, *J. Appl. Phys.* **1995**, *78*, 1364.
[17] M. R. Fitzsimmons, J. A. Eastman, R. A. Robinson, A. C. Lawson, J. D. Thompson, R. Movshovich, J. Satti, *Phys. Rev. B* **1993**, *48*, 8245.
[18] W. S. Zhang, E. Brück, Z. D. Zhang, O. Tegus, W. F. Li, P. Z. Si, D. Y. Geng, K. H. J. Buschow, *Physica B: Condens. Matter* **2005**, *358*, 332.
[19] J. P. Toennies, A. F. Vilesov, *Angew. Chem., Int. Ed.* **2004**, *43*, 2622.
[20] A. Boatwright, C. Feng, D. Spence, E. Latimer, C. Binns, A. M. Ellis, S. Yang, *Faraday Discuss.* **2013**, *162*, 113.
[21] A. Volk, P. Thaler, M. Koch, E. Fisslthaler, W. Grogger, W. E. Ernst, *J. Chem. Phys.* **2013**, *138*, 214312.
[22] P. Thaler, A. Volk, D. Knez, F. Lackner, G. Haberfehlner, J. Steurer, M. Schnedlitz, W. E. Ernst, *J. Chem. Phys.* **2015**, *143*, 134201.
[23] P. Carra, B. T. Thole, M. Altarelli, X. Wang, *Phys. Rev. Lett.* **1993**, *70*, 694.
[24] C. T. Chen, Y. U. Idzerda, H. J. Lin, N. V. Smith, G. Meigs, E. Chaban, G. H. Ho, E. Pellegrin, F. Sette, *Phys. Rev. Lett.* **1995**, *75*, 152.
[25] E. Goering, *Philos. Mag.* **2005**, *85*, 2895.
[26] V. Corradini, F. Moro, R. Biagi, U. del Pennino, V. De Renzi, S. Carretta, P. Santini, M. Affronte, J. C. Cezar, G. Timco, R. E. P. Winpenny, *Phys. Rev. B* **2008**, *77*, 014402.
[27] P. Ohresser, H. Bulou, S. S. Dhesi, C. Boeglin, B. Lazarovits, E. Gaudry, I. Chado, J. Faerber, F. Scheurer, *Phys. Rev. Lett.* **2005**, *95*, 195901.
[28] H. Wende, A. Scherz, C. Sorg, K. Baberschke, E. K. U. Gross, H. Appel, K. Burke, J. Minár, H. Ebert, A. L. Ankudinov, J. J. Rehr, *AIP Conf. Proc.* **2007**, *882*, 78.
[29] K. Binder, *Applications of the Monte Carlo Methods in Statistical Physics*, Springer-Verlag, Berlin, Heidelberg, Germany **1984**.
[30] S. Mørup, C. Frandsen, *Phys. Rev. Lett.* **2004**, *92*, 217201.
[31] D. E. Madsen, S. Mørup, *Phys. Rev. B* **2006**, *74*, 014405.
[32] G. Brown, A. Janotti, M. Eisenbach, G. M. Stock, *Phys. Rev. B* **2005**, *72*, 140405R.
[33] A. Kautsch, M. Koch, W. E. Ernst, *Phys. Chem. Chem. Phys.* **2015**, *17*, 12310.
[34] G. Kresse, J. Furthmuller, *Comput. Mater. Sci.* **1996**, *6*, 15.
[35] S. S. Sartiman, N. F. Djaja, R. Saleh, *Mater. Sci. Appl.* **2013**, *4*, 528.
[36] K. N. Trohidou, X. Zianni, J. A. Blackman, *J. Appl. Phys.* **1998**, *84*, 2795.
[37] K. N. Trohidou, M. Vasilakaki, *J. Phys. D: Appl. Phys.* **2008**, *41*, 134006.
[38] J. P. Perdew, K. Burke, M. Ernzerhof, *Phys. Rev. Lett.* **1996**, *77*, 3865.
[39] P. E. Blochl, *Phys. Rev. B* **1994**, *50*, 17953.
[40] H. Monkhorst, J. Pack, *Phys. Rev. B* **1976**, *13*, 5188.